Published in final edited form as:
J Control Release. 2009 June 5; 136(2): 99–109. doi:10.1016/j.jconrel.2009.01.016.

Intramuscular Drug Transport Under Mechanical Loading: Resonance Between Tissue Function and Uptake

Peter I. Wu[a,1], **Sara Minisini**[b], and **Elazer R. Edelman**[a,c]

a *Biomedical Engineering Center, Harvard-MIT Division of Health Sciences and Technology, Massachusetts Institute of Technology, E25-438 Cambridge, Massachusetts 02139, USA*

b *MOX – Modeling and Scientific Computing, Department of Mathematics, Politecnico di Milano, Via Bonardi 9, 20133 Milano, Italy*

c *Cardiovascular Division, Department of Medicine, Brigham and Women's Hospital, Harvard Medical School, Boston, Massachusetts 02115, USA*

Abstract

Dynamic architecture and motion in mechanically active target tissues can influence the pharmacokinetics of locally delivered agents. Drug transport in skeletal muscle under controlled mechanical loads was investigated. Static (0–20%) and cyclic (±2.5% amplitude, 0–20% mean, 1–3 Hz) strains and electrically paced isometric contractions (0.1–3 Hz, 0% strain) were applied to rat soleus incubated in 1 mM 20 kDa FITC-dextran. Dextran penetration, tissue porosity, and active force-length relationship over 0–20% strain correlated (r = 0.9–1.0), and all increased 1.5-fold from baseline at 0% to a maximum at 10% (L_o), demonstrating biologic significance of L_o and impact of fiber size and distribution on function and pharmacokinetics. Overall penetration decreased but relative enhancement of penetration at L_o increased with dextran size (4–150 kDa). Penetration increased linearly (0.084 mm/Hz) with cyclic stretch, demonstrating dispersion. Penetration increased with contraction rate by 1.5-fold from baseline to a maximum at 0.5 Hz, revealing architectural modulation of dispersion. Impact of architecture and dispersion on intramuscular transport was computationally modeled. Mechanical architecture and function underlie intramuscular pharmacokinetics and act in concert to effect resonance between optimal physiologic performance and drug uptake. Therapeutic management of characteristic function in tissue targets may enable a physiologic mechanism for controlled drug transport.

Keywords

Muscle; Strain; Contraction; Transport; Pharmacokinetics

1. Introduction

Mechanically active tissues such as skeletal muscle present a unique pharmacokinetic environment in which transport of locally delivered drug can be influenced by not only physicochemical interactions, but also dynamic architectural configurations and mechanical

1Corresponding author. Massachusetts Institute of Technology, Room E25-442, Cambridge, Massachusetts 02139, USA. Tel.: +1-617-258-8893; fax: +1-617-253-2514. E-mail address: E-mail: pkungwu@mit.edu (P. Wu).

function. The continuous network of force-transmitting and connective perimysial and endomysial collagen fibers [1] between myofibers can hinder interstitial diffusion in a strain-dependent manner. Dynamic physical effects such as intramuscular pressure, fluid redistribution, and structural deformations [2,3] during mechanical function can alter transport kinetics. Whereas local delivery strategies minimize systemic losses and enable efficient administration of therapies to target tissues [4,5], ultimate drug distribution and pharmacologic effect are determined by target tissue pharmacokinetics. A quantitative understanding of intramuscular transport forces is critical for clinically motivated strategies like therapeutic angiogenesis, which seeks to locally deliver pro-angiogenic factors to ischemic muscles [4,6, 7].

Studies have investigated how strain or contraction in whole skeletal muscles affects total uptake of glucose [8–10], lactate [11], phosphate [12], calcium [13,14], and fatty acid [15]. However, they have predominantly elucidated the pharmacokinetic influence of activity-dependent metabolism on substrate uptake. This present study applied a rigorous, quantitative framework to investigate the characteristic and synergistic impact of functional architecture and mechanical forces on intramuscular transport of locally delivered soluble macromolecules. Having previously demonstrated that cyclic mechanical loading influences drug distribution based on the dictates of muscle geometry, we systematically investigated the transport effects of static and cyclic strain and isometric contraction, and their unique correlation with structure and function. The mechanisms at hand were validated through computational models.

2. Methods

2.1 Surgical Protocol

Experiments were conducted within the animal welfare regulations and guidelines of Massachusetts. Male Sprague-Dawley rats (450–470 g, Charles River) were administered 1000 U of Heparin (Webster Veterinary) via intraperitoneal injection 5 min before euthanasia with inhaled CO_2. Thoracotomy was performed immediately after euthanasia, and 60 ml of Krebs-Henseleit-Butanedione Monoxime (KH-BDM) (in mM: 118.1 NaCl, 4.7 KCl, 2.5 $CaCl_2$, 1.2 $MgSO_4$, 1.2 KH_2PO_4, 25 $NaHCO_3$, 11.1 Glucose, supplemented with 1 Sodium Pyruvate, 1 Isoleucine, 1 Leucine, 1 Valine, and 5 BDM at pH 7.4) (all components from Sigma, cell culture tested) oxygenated with 95% O_2-5% CO_2 was infused down the aorta to relax and preserve tissues of the lower extremities during surgery.

The soleus was measured, isolated, and resected with its tendons and segments of the calcaneus and fibula intact as described previously [16]. The *in situ* length of the soleus, measured using a Mitutoyo Digimatic caliper with ± 0.01 mm precision between the proximal and distal myotendinous junctions while flexing the knee and ankle at 90° and referred to as the nominal length, corresponded to the *initial* length, at which passive resistance to stretch first occurs. Because rats were selected from a narrow weight range, all soleus muscles were of equal size and measured 28 mm in nominal length. After excision, muscles equilibrated in oxygenated KH that chilled on ice for 15 min before mechanical loading. For electrically paced groups, KH was used in all parts of the surgical protocol.

2.2 Mechanical Loading and Drug Delivery

All static and cyclic strains were applied on pairs of whole soleus muscles using a custom-built mechanical loading system described previously [16]. For all loading conditions described below, muscles were stretched for 1 h in 16 ml of 1 mM 20 kDa FITC-dextran (Sigma, No. FD20) in KH. Drug source was kept oxygenated, at room temperature, and well-mixed by magnetic stir bar.

2.2.1 Static Strain—Muscles (n = 6) were held stretched to 0%, 5%, 10%, 15%, or 20% strain. 0% strain corresponds to nominal length, 5% corresponds to 105% of the nominal length, etc. 10% strain was found previously to correspond to *optimal length* L_o. Muscles (n = 6) were similarly stretched to 0%, 10%, or 20% and incubated in 1 mM of 4 kDa or 150 kDa FITC-dextran (Sigma, No. FD4 & FD150).

2.2.2 Cyclic Stretching—Muscles (n = 6) were loaded to sinusoidal strains with an amplitude of 2.5% of the nominal length about mean strains of 0%, 5%, 10%, or 20% at 1, 2, or 3 Hz. Muscles (n = 6) were also loaded at 1 Hz for 1 h, 2 Hz for 30 min, and 3 Hz for 20 min at both 0% and 5% strain.

2.2.3 Contractions—Muscles (n = 6) were continuously paced by electric field stimulation to produce isometric twitch contractions at nominal length at a rate of 0.1, 0.5, 1, 2, or 3 Hz. Biphasic stimulus (15 V, 50 ms pulse) was applied by 2 stainless steel foil plates situated in the drug bath at either end of the static loading assembly, spanning a separation distance of 10 cm. Stimulus was generated using a National Instruments DAQPAD-6062E data acquisition board controlled by LabView 7.0. Incubated muscles produced a minimum isometric twitch force of 0.19 N for at least 2 h and maintained contractile activity at 3 Hz for at least 1 h.

2.3 Tissue Processing and Measurement of Drug Transport

After loading, muscles were rinsed twice in 15 ml of fresh KH and snap-frozen at nominal length in −145°C Isopentane. 8 μm thickness axial cross-sections from the midpoint of muscles were cut using a Leica CM1850 cryotome. FITC-dextran was imaged using epifluorescence microscopy (Leica DMRA2, 50× magnification, Hamamatsu ORCA 286, Metamorph 6.3, ex: 450–490 nm bandpass/em: 515 nm longpass). An exposure rate was chosen that eliminated tissue autofluorescence and intensity saturation of the system by the drug source. Images were analyzed using Matlab. Preliminary calibration confirmed linearity between image fluorescence intensities and tissue drug concentrations for 0.01 mM–1 mM bulk source concentrations of 20 kDa FITC-dextran. Unidirectional drug penetration at the planar surface of the muscle axial cross-section was quantified. Intramuscular penetration depth was defined as the perpendicular distance from the surface at which fluorescence intensity decreased to 5% of the surface intensity. Effective diffusivity, D, associated with measured penetration depth, x, was calculated based on the equation for diffusion into a semi-infinite solid, $D=\frac{x^2}{4\cdot t\cdot(\mathrm{erf}^{-1}(0.95)^2)}$.

2.4 Histology and Tissue Architecture

Muscles (n = 6) were excised and immediately snap-frozen at 0%, 5%, 10%, 15%, or 20% strain. 8 μm axial cross-sections from the midpoint of muscles were cut and stained with Hematoxylin and Eosin (HE) (Sigma). Light microscopy images (100×) were processed using CellProfiler [17] in Matlab. Tissue porosity (ϕ, ratio of interstitial space area to total area), average myofiber cross-sectional area, and myofiber density (number of fibers per unit area) were quantified at each strain. Tissue degradation and injury were found to depend only on time, thus baseline architecture was consistent among all samples incubated for the same duration, and differences in drug transport could be attributed to the distinct influences of mechanical loading.

2.5 Statistical Analysis

Student's t-Test, Single Factor Analysis of Variance (ANOVA), and Two-Factor ANOVA with Replication were applied to derive significance in empirical transport results.

2.6 Mathematical Model

2.6.1 Static Case—Homogenization, a mathematical technique used previously in models of cardiac electrical conductivity, effective intercellular diffusion through cardiac cells coupled by gap junctions [18], and effective transport in brain tissue [19], was applied to model the relationship between effective diffusivity and strain-dependent tissue porosity in the soleus. Homogenization accounts for spatial variations in drug concentration on the cellular level to characterize drug concentration profiles on the tissue level to derive effective transport. Intramuscular effective diffusivity, D_{eff}, of inert, soluble macromolecules like dextran in the interstitium was defined as [19]:

$$D_{eff}=(D_1 \cdot D_2) \cdot D_w \tag{1}$$

where D_w is the free diffusivity of drug in water, and reducing factor $D_1 \cdot D_2 \leq 1$. D_1 accounts for porosity ϕ, fiber geometry, and arrangement and relates effective diffusivity to interstitial diffusivity independently of drug molecular weight (MW). D_2, which accounts for interstitial fluid characteristics and is independent of ϕ when drug size is considerably smaller than the interspacing between myofibers, was equal to 1 because interstitial fluid was assumed to be water *in vitro*. Thus, D_{eff} was determined by modeling D_1.

Because the uniaxial soleus was exposed to constant drug source uniformly along its length during loading, transport in the radial, or cross-fiber, direction was investigated. D_1 was determined using a homogenization procedure on the diffusion equation within the tissue (Appendix A) [18–20]. The computational domain describing the axial cross-section of the soleus was a porous medium (lattice) shown in Fig. 1. The direction of macroscopic drug diffusion, defined by a vector e, ran in the negative y-direction and reproduced drug penetration across myofibers. Diffusion in the direction of e was determined by solving the Laplacian equation in the reduced lattice domain Ω (Fig. 1B, *inset*):

$$\nabla^2 \chi = 0 \tag{2}$$

where the function χ represents the small periodic component of the macroscopic drug concentration field under boundary conditions determined by e. These boundaries consisted of symmetric and periodic conditions at the interstitial borders between lattice domains (Γ_1) that were respectively parallel or perpendicular to e (Fig. 1C) and the Neumann condition:

$$\underline{n} \cdot \nabla \chi = \underline{n} \cdot \underline{e} \tag{3}$$

on myofiber surfaces (Γ_2). D_1 in the direction of e was:

$$D_1 = \frac{D_{eff}}{D_w} = \frac{1}{A} \int_{\Omega} (1 - \underline{e} \cdot \nabla \chi)\, d\Omega \tag{4}$$

where A is the area of Ω. Eq. (2) was solved using COMSOL Multiphysics®. Porosity changes were modeled by changing diamond (myofiber) size while maintaining their lattice positions fixed and the total area of the lattice constant. Values used for ϕ at each static strain were taken from empirical measurements of porosity in histologic images.

A regular lattice domain was used to model the homogeneous myofiber and interstitial architecture produced by 0% and 20% strains (Fig. 1B). A widened interstitial channel aligned

with e was introduced to model the inhomogeneous fiber arrangement with wide interstitial spaces produced by 5%, 10%, and 15% strains (Fig. 1E). The regular lattice portion in this domain was modeled with porosity equal to local porosity measured in a single fascicle. The enlarged channel width was modeled so that average porosity of the entire domain equaled average porosity measured in the entire histologic cross-sectional image.

2.6.2 Dynamic Case—The uniaxial soleus was modeled as a cylinder with circular cross-section. A two-dimensional model was used to investigate the dispersive effects [21–23] of cyclic radial deformations on radial drug penetration. Drug transport was described by the diffusion equation on a continuous domain, $\Omega_D(t)$, characterizing the entire axial cross-section of the muscle:

$$\frac{\partial c}{\partial t} - D_{eff}\nabla^2 c = 0 \quad \text{in } \Omega_D(t) \tag{5}$$

where c is the drug concentration field, D_{eff} is the empirical effective diffusivity associated with static stretch to the mean strain, and $\Omega_D(t)$ moves according to:

$$\Omega_D(t) = \pi r(t)^2 = \pi(Rn)^2(1+\alpha\sin(\omega t))^2 \tag{6}$$

where r(t) is the radius of the cross-section, α is the radial strain amplitude centered about the mean radius Rn (with n = 0, 5, 10, 20), and ω is the radial frequency of pulsation or deformation (where ω = 2π, 4π, 6π rad/sec). Theoretical values of the radius and radial deformations resulting from axial stretch were calculated from tensile strains applied experimentally based on conservation of volume and tissue incompressibility (Poisson ratio = 0.5) [24] (Appendix B).

Using the Arbitrary Lagrangian Eulerian (ALE) formulation [25], Eq. (5) became:

$$\frac{\partial c}{\partial t} - D_{eff}\nabla^2 c - \underline{w}\cdot\nabla c = 0 \quad \text{in } \Omega_D(t) \tag{7}$$

where w is the velocity of $\Omega_D(t)$ (Appendix C). Eq. (7) was solved using COMSOL to obtain the drug concentration profile in the muscle cross-section after 1 h of transport. Drug concentration at the boundary of $\Omega_D(t)$ was a constant value fixed at 1 and penetration depth was taken as the distance from the boundary at which concentration decreased to 0.05.

3. Results

3.1 Static Strain, Cyclic Stretching, and Contractions

Tensile strain increased drug penetration and effective diffusivity (Fig. 2A). Penetration increased by 1.45-fold to a maximum at 10% strain and fell off thereafter. This penetration profile correlated with the isometric twitch force-length relationship of the muscle (r = 0.87, Fig. 2B), suggesting architectural state is an important determinant of drug transport in contractile tissues. Maximal penetration at 10% thus correlated with optimal length L_o, as defined by peak twitch force. Overall dextran penetration decreased with increasing molecular weight and size (Fig. 2C). Whereas 10% strain enhanced penetration past that at 0% by an increasingly greater distance for smaller molecules that are less sterically hindered, relative enhancement at 10% was most evident for larger molecular sizes that encounter greater steric hindrance (Fig. 2D).

Cyclic tensile loading over 1–3 Hz consistently enhanced drug penetration at each mean strain above that produced by static strain alone by an average of 0.084 mm/Hz (Fig. 3A and B). Thus, the penetration profile across mean strains for each loading frequency followed the same trend dictated by static strain (Fig. 3C). As penetration was linearly dependent on loading rate, it was directly dependent on the number of cycles of loading. Penetration at each mean strain was identical over a range of frequencies when the product of loading duration and frequency was kept the same, such that all tissues were subjected to 3600 cycles of loading (Fig. 3D).

Isometric twitch contractions of 0.1–3 Hz at nominal length enhanced drug penetration above that occurring with static strain (Fig. 4). Penetration increased with contraction rate by 1.52-fold to a maximum at 0.5 Hz and fell off thereafter (T-test, $p<0.05$).

3.2 Tissue Architecture

Minimum interstitial spacing between myofibers in histologic images, 0.43 μm, was comparable to experimental values (~ 0.1 μm) found previously [26]. Myofiber arrangement was homogeneous at 0% and 20% strains, but was interrupted by enlarged intercellular channels (along fascicular borders) of 11.1–34.7 μm width at 5%, 10%, and 15% strains (Fig. 5A).

Tissue porosity (Fig. 5B) at 0% strain, 0.12 ± 0.01, was in agreement with extracellular inulin space (0.12 ± 0.01) found previously in rat soleus [27]. Imprecision in porosity measurements may arise from cross-sections taken perpendicular to the muscle body rather than to the myofibers, which have a 6° pennation angle to the muscle axis. However, discrepancy between sectional cuts and such a small pennation angle and the minor changes it undergoes with muscle stretch would only result in a 0.5% error in porosity that would already be encompassed by the 8 to 11% standard deviation in measurements. Porosity increased with tensile strain by 1.5-fold to a maximum at L_o and fell off thereafter. That this porosity profile correlated with the isometric twitch force-length relationship ($r = 0.87$) and exactly with the penetration profile over static strain ($r = 1$) suggests that tissue porosity, which is the architectural correlate of functional state, is a direct determinant of drug transport in contractile tissues.

Whereas average cross-sectional area of myofibers decreased to an asymptotic value, fiber density increased from an asymptotic value with increasing strain (Fig. 5C). Both profiles inflected symmetrically at L_o, indicating the significant correspondence of architectural state with muscle function and pharmacokinetics. Change in porosity was validated by the nonlinear relationship between fiber density and average area, suggesting that porosity, fiber area, and fiber density are distinct parameters that change interrelatedly to affect the transport environment.

3.3 Numerical Results

Transport under static strain was influenced by the combined effects of porosity and fiber arrangement. Transport through the homogeneous fiber arrangement under 0% and 20% strains was accurately characterized by diffusion perpendicular to the axis of a homogeneous lattice arrangement (Fig. 6A, *Isotropic Medium*, lower limit of diffusivity) and the relationship, $D_{eff}/D_w = 0.58\phi$. Transport through the inhomogeneous fiber arrangement under 5%, 10%, and 15% strains was accurately characterized by diffusion across a lattice arrangement with an enlarged channel aligned in the direction of transport (*Medium with Channel*) and the relationship, $D_{eff}/D_w = 1.044\phi - 0.0442$, which had a slope that approximated the upper limit of diffusivity. Diffusion was greater with the presence of an enlarged channel (Fig. 1E) than across a homogeneous arrangement (Fig. 1B) with uniformly widened interspaces and an equivalent average porosity.

Dispersion was computationally validated by the linear dependence of radial drug penetration on the frequency of cyclic radial loading, independent of mean strain (Fig. 6B).

4. Discussion

Characteristic dynamic architecture, motion, and contraction in skeletal muscle targets significantly influenced intramuscular pharmacokinetics. This study investigated the impact of controlled mechanical loading on inert dextran penetration in soleus muscle. Computational models of interstitial drug transport elucidated the architectural and dispersive influences underlying the pharmacokinetic effects of static and dynamic strain.

4.1 Static Strain

Strain from 0% to 20% spans the physiologic range of muscle function and extensibility [28]. Drug transport within this range reflected the pharmacokinetic environment dictated by physiologic architectural configurations and function. The exact correlation between effective diffusivity and porosity over static strain confirmed extracellular transport of soluble dextran [29] and indicated muscle strain influences transport through impact on structural porosity.

Whereas previous studies have shown passive stretch unilaterally increases glucose uptake [8], we elucidated an architecturally defined optimal setpoint rendering maximal drug penetration at the physiologic configuration for peak muscle performance, optimal length L_o. Characteristic changes in fiber size, density, and organization suggest strain-dependent porosity, which mediates this parabolic increase in transport, resulted from the asynchronous progression of conservation of myofiber volume and myofiber packing density with strain. Through conservation of volume, myofibers undergo continuous reduction in cross-sectional size with elongation. Upon initial stretch, fiber thinning opens interstitial space, increasing porosity and transport. Interstitial enlargement is accompanied by space and myofiber redistribution along fascicular borders, likely corresponding to muscle volume changes that occur during activity[30]. Thus, increased tissue-averaged porosity results from not only homogeneous space enlargement, but also myofiber redistribution that can connect interstitial spaces and precipitate the formation of enlarged channels with low tortuosity. As demonstrated by our static model, these widened channels greatly facilitated diffusion and rendered maximal penetration at L_o. With elongation past L_o, fiber density increases as the entire muscle bundle tightens and increasingly thin fibers compact together, resulting in contraction of interstitial space, recession of open channels, and reduction of porosity and diffusion. These changes likely correspond to muscle volume decrease [30] and intramuscular and interstitial pressure increase [31] that occur with passive stretch beyond L_o. Through the structural changes depicted by the asymptotic profiles of fiber size and density, porosity was modulated predominantly by the local effects of fiber size at strains less than L_o, and global effects of fiber distribution at strains greater than L_o.

Correlation between transport, porosity, and the active force-length relationship, whereby all three increased 1.5-fold from baseline to a maximum at L_o, suggests the physiologic nexus ascribed to L_o, whose architectural configuration enables optimal interface between the tissue and its external environment. The profiles of fiber area and density over 0–20% strain indicate architectural configurations within the physiologic range of muscle extensibility and function are defined by the passive material limits of myofibers and connective tissue. Fiber density started from a minimum asymptote at the initial length, indicating the resting state of fiber aggregation and maximal mechanical compliance of the muscle bundle rendered by the connective collagen fascial framework. Fiber size reached a minimum asymptote by 20% strain, suggesting the extent of myofiber incompressible elasticity. Between these physical limits, the profiles of both fiber size and density inflected critically at L_o, where these parameters correlated maximal porosity with optimal mechanical performance. Perhaps

maximal extracellular space is the structural measure of and functionally related to optimal contractile efficiency in that it enables increased vascular perfusion by reducing intramuscular pressure [32,33] or optimizes the available volume surrounding myofibers for swelling and thickening [3,34] during contraction.

4.2 Dextran Molecular Weight

Size-dependent mobility of dextran in the interstitium reflected variable steric interaction with architecture. The continuous, dense network of collagen fibers forming the endomysium and perimysium sterically hinders soluble drug diffusion [35]. As this network provides support and force transmission between myofibers [1], structural deformations associated with mechanical loading can modulate the screening effect on drug transport mediated by the network. The collagen fibers, which are randomly orientated in relaxed muscle, align circumferentially to myofibers with muscle shortening and axially with muscle elongation [36–38]. Because permeability is greater through a periodic rather than a random distribution of obstacles [39], alignment of collagen fibers with strain increases interstitial permeability. These changes impact mobility within the accessible volume to drug defined by macro-scale tissue-averaged porosity. The extent of steric hindrance and interstitial mobility was demonstrated by the penetration of dextrans of various sizes.

The architectural configuration at L_o defines an interstitial collagen and myofiber alignment that optimally reduces steric hindrance and enhances penetration. This transport effect likely varies, like L_o and its associated maximal force, among different muscles. Physical properties of the drug, namely molecular size, further dictate the ultimate effect on penetration presented by intramuscular fiber alignment. Diffusivity increased with decreasing dextran size. At the lowest molecular weights, steric hindrance likely becomes negligible because the effective radius of such drugs is substantially smaller than the minimal barrier to diffusion posed by fiber alignment. Penetration of such small molecules would be the maximum achievable under the static, architecturally defined transport environment and could only be enhanced further by dynamic forces such as dispersion or convection induced by muscle activity. Whereas net penetration decreased with increasing dextran size, the relative enhancement of penetration at L_o increased. For larger molecules like 150kDa dextran, penetration at L_o is significant compared to penetration at 0% strain. For this and larger sizes, penetration into muscle is minimal under static conditions and enhancement at L_o is therefore significant. Molecules of even greater size may be altogether sterically excluded even at L_o and thus also derive no enhancement of penetration from the dynamics of muscle activity.

4.3 Cyclic Stretching

In the absence of an external convective force driving bulk fluid flow into the muscle, and particularly as drug penetration proceeded against an increasing intramuscular pressure gradient during stretch [33], enhancement of penetration by oscillatory loading was unlikely the result of bulk convection. Dynamic loading may cyclically expose drug to strain-dependent architectural configurations with larger accessible volumes and result in a greater time-averaged porosity that increases penetration. However, this mechanism depends only on static architectural states, and average porosity over a single loading cycle remains the same regardless of loading frequency. Enhancement of transport that readily superposed on the static strain transport profile suggests a dynamic process rather than further reduction of architectural exclusion. Dispersion is likely the predominant driving force because enhancement of penetration was linearly dependent on loading frequency and independent of mean strain.

Dispersion impacts the transport kinetics of soluble drug by increasing transport beyond molecular diffusion alone [21]. Axial strain translates into radial or lateral deformation of the whole muscle due to conservation of volume mediated through lateral force transmission by

interstitial connective tissues [40,41]. Whole muscle structure is stabilized by mechanical force balance, or isometric tension, between the myofiber cytoskeleton and interstitial connective tissue. This interstitial connective tissue is comprised of interconnected lattice networks of tension-resistant collagen fibers that form a fascial framework consisting of the endomysium that ensheathes individual myofibers, the perimysium that bundles groups of myofibers into fascicles, and the epimysium that envelops the entire muscle and connects to the tendons. The fascial framework plays a significant role in reinforcing muscle structure, mediating passive elasticity and tensional strength, and transmitting forces among adjacent myofibers and to tendons predominantly in the form of shear stress. Such structural and functional integrity is mediated by continuity of force transmission from contractile myofilaments and cytoskeletal elements in myofibers across the sarcolemma and basal lamina to the fascial framework. Myofibers transmit force to this framework both through their ends and along their entire lateral surfaces via membrane associated sites such as costameres/focal adhesions, dystroglycan/sarcoglycan complexes, and perimysial junctional plates [41] that bind to laminin in the basal lamina and collagen in the endomysium and perimysium, which then distribute this force among myofibers before transmitting it evenly across the entire myotendinous junction to the tendon. Thus, the whole muscle is structured as a mechanically integrated complex consisting of parallel systems of tensile elements, myofibers and the fascial framework that dynamically bear compression or tension depending on loading condition, that are anchored at membrane sites and the myotendinous junction, where shear transmission is concentrated. Tensional continuity within the muscle complex and conservation of volume in muscle tissues render the response of the whole muscle to external mechanical stresses. With muscle stretch, the fascial framework sustains axial tension and compresses synchronously stretched and thinning myofibers to render whole muscle lateral deformation [42].

Cyclic displacement of myofibers compresses and expands extracellular space and imposes normal and shear forces on interstitial fluid, resulting in pulsatile agitation and movement of soluble drug in the absence of bulk convection. Such agitation can disperse or spread drug in a rate-dependent manner over a greater extracellular volume, thereby driving greater penetration.

4.4 Contractions

Unlike studies of contraction-induced substrate transport, which have shown that contraction increases glucose transport based on metabolic changes [9,43], or that glucose [10] or calcium [13] uptake scales unilaterally with frequency of contraction, we elucidated a functionally-associated optimal setpoint rendering maximal drug penetration at 0.5 Hz isometric contractions at nominal length. Cyclic dynamics alone can increase penetration through dispersive effects that scale with frequency. However, decreasing penetration with contraction rates above 0.5 Hz suggests competing transport effects that predominated at higher frequencies. Contraction influences transport through the combined effects of active muscle function and architectural configuration. We propose the bimodal trend in penetration with contraction rate results from time-dependent competition between dispersion and steric hindrance, whereby dispersion predominates below and steric hindrance predominates above a critical contraction rate determined by the isometric muscle length.

Even under isometric conditions, contraction-associated myofiber thickening [30] occurs as a result of cytoplasmic volume displacement from the smaller end-regions of myofibers toward the middle. Fiber thickening produces transverse forces and a squeezing effect that decreases porosity and increases interstitial fluid pressure [31,32]. Fiber swelling resulting from interstitial water movement into the fibers [34] reduces interstitial space available for drug in the absence of vascular perfusion *in vitro* [30,44]. These effects resist drug penetration. Fiber relaxation after contraction results in fiber thinning that re-opens interstitial space, restores

porosity, and relieves interstitial fluid pressure. Cyclic transitions between the contracted and relaxed architectural states create dispersive effects that increase drug penetration. With contraction rates below 0.5 Hz, muscle architecture spends a greater percentage of time in the relaxed state, which enables dispersive effects to dominate. This in agreement with findings that reveal low frequency isometric contractions (3 contractions/min) increase both inulin uptake and washout in papillary muscle [45]. With contraction rates above 0.5 Hz, extending to the limit of complete tetanus, muscle architecture spends an increasingly greater percentage of time in the contracted state, which exposes drug to a greater temporal resistance to penetration and progressively swelling fibers. At these frequencies, the effects of increased temporal steric hindrance and elevated interstitial pressures outweigh the effects of dispersion, thereby precluding enhancement of drug penetration.

As static strain affected tissue porosity, it is likely that this contraction rate dependence of maximal penetration shifts with the isometric length of the muscle. This possibility is supported by the finding that the extent of contraction-associated muscle volume decreases varies with initial length of the muscle, becoming greater with greater initial lengths beyond L_o [30]. We predict the optimal frequency may increase with isometric lengths that effect greater porosities.

4.5 Perspectives

Our findings elucidate opportunities for diagnostic techniques and therapeutic windows for improved drug delivery to mechanically active tissues. Static strain and isometric contraction enable adaptable physiologic mechanisms for modulating or maximizing drug transport. Strain-dependent steric hindrance demonstrates a physiologic means for selective drug uptake. Strain to L_o could facilitate maximal penetration of low molecular weight drugs, or filter drugs delivered in mixed formulations to allow selective entry of smaller drugs at desired temporal windows. Further insight from the calculated upper limit of diffusion indicates transport across fibers is the limiting direction in drug distribution. As axial drug transport outweighs radial penetration, focal application of drug along the muscle axis may possibly achieve delivery to the entire length of the muscle but come at the expense of reduced drug penetration into the tissue. Dispersion through cyclic strain presents a physically controlled and easily scalable mechanism that can be readily applied in combination with architectural control of tissue porosity to increase or modulate drug penetration. These physiologic mechanisms engender physical therapies that stretch or stimulate muscle targets as strategies for improving controlled drug delivery. Our quantitative findings may be readily applied to address the current need to optimize local drug delivery strategies for promising, clinically motivated therapies like therapeutic angiogenesis [6] to treat increasingly prevalent peripheral vascular disease, in which ischemic lesions in skeletal muscle are spatially focal, therapeutic windows are narrow [46,47], therapeutic response is complex [48], biologic half-lives of delivered growth factors are short [49], and systemic side-effects of therapies are detrimental [50].

The relationship between drug uptake and target tissue functional architecture and activity presents new insights on the significance of biologic form and function. Correlation of maximal drug penetration with optimal muscle function reflects biologic design that harmonizes the reciprocal interaction between tissue and its physical environment. This design may further reflect the potential for L_o to be a structural setpoint that uniquely modulates myofiber mechanochemical transduction and integration [51] whereby strain supported by the myofiber cytoskeleton and related transmembrane receptors or stretch-sensitive channels at L_o influences cellular sensitivity and response to extracellular factors. Just as optimal biologic responsiveness to pulsatile fluid flow in different cell types occurs at the inherent frequencies to which they are exposed in their physiologic environments [52], optimal intramuscular pharmacokinetics center within the range of physiologic tissue extensibility and operation at the length of maximal force generation and contractile efficiency. Functionally dictated optimal

pharmacokinetic conditions suggest the existence of potential therapeutic windows that correspond to unique setpoints in the physiologic operating range of all target tissues and organs.

5. Conclusions

Mechanically active tissues present a dynamic pharmacokinetic environment in which permeability and drug transport are influenced by the interrelated effects of architectural configuration and functional dynamics. Dispersive effects of cyclic loading can be superposed on the structural dependence of tissue permeability to enhance drug penetration. Correlation of both L_o and an architecturally modulated optimal contraction rate with a respective maximal penetration elucidates the resonant nature of skeletal muscle interaction with the physical environment. Such biologic design elucidates new strategies for controlled drug delivery that harness the pharmacokinetic impact of functional architecture in target tissues.

Acknowledgements

These studies were supported by graduate fellowships from the Department of Defense and the Whitaker Foundation for Biomedical Engineering to Peter I. Wu, the “Progetto Roberto Rocca” MIT-Politecnico di Milano collaboration to Sara Minisini, and a research grant from the National Institutes of Health (NIH/NIGMS R01/HL049039) to Elazer R. Edelman.

References

1. Jarvinen TA, Jozsa L, Kannus P, Jarvinen TL, Jarvinen M. Organization and distribution of intramuscular connective tissue in normal and immobilized skeletal muscles. An immunohistochemical, polarization and scanning electron microscopic study. J Muscle Res Cell Motil 2002;23(3):245–254. [PubMed: 12500904]
2. Savelberg HH, Willems PJ, Baan GC, Huijing PA. Deformation and three-dimensional displacement of fibers in isometrically contracting rat plantaris muscles. J Morphol 2001;250(1):89–99. [PubMed: 11599018]
3. Trombitas K, Baatsen P, Schreuder J, Pollack GH. Contraction-induced movements of water in single fibres of frog skeletal muscle. J Muscle Res Cell Motil 1993;14(6):573–584. [PubMed: 8126217]
4. Guan J, Stankus JJ, Wagner WR. Biodegradable elastomeric scaffolds with basic fibroblast growth factor release. J Control Release 2007;120(1–2):70–78. [PubMed: 17509717]
5. Ungaro F, Biondi M, d’Angelo I, Indolfi L, Quaglia F, Netti PA, La Rotonda MI. Microsphere-integrated collagen scaffolds for tissue engineering: effect of microsphere formulation and scaffold properties on protein release kinetics. J Control Release 2006;113(2):128–136. [PubMed: 16787679]
6. Messina LM, Brevetti LS, Chang DS, Paek R, Sarkar R. Therapeutic angiogenesis for critical limb ischemia: invited commentary. J Control Release 2002;78(1–3):285–294. [PubMed: 11772469]
7. Gu F, Amsden B, Neufeld R. Sustained delivery of vascular endothelial growth factor with alginate beads. J Control Release 2004;96(3):463–472. [PubMed: 15120902]
8. Ito Y, Obara K, Ikeda R, Ishii M, Tanabe Y, Ishikawa T, Nakayama K. Passive stretching produces Akt- and MAPK-dependent augmentations of GLUT4 translocation and glucose uptake in skeletal muscles of mice. Pflugers Arch 2006;451(6):803–813. [PubMed: 16244881]
9. Sandstrom ME, Zhang SJ, Westerblad H, Katz A. Mechanical load plays little role in contraction-mediated glucose transport in mouse skeletal muscle. J Physiol 2007;579(Pt 2):527–534. [PubMed: 17185338]
10. Aslesen R, Engebretsen EM, Franch J, Jensen J. Glucose uptake and metabolic stress in rat muscles stimulated electrically with different protocols. J Appl Physiol 2001;91(3):1237–1244. [PubMed: 11509521]
11. Tonouchi M, Hatta H, Bonen A. Muscle contraction increases lactate transport while reducing sarcolemmal MCT4, but not MCT1. Am J Physiol Endocrinol Metab 2002;282(5):E1062–1069. [PubMed: 11934671]

12. Abraham KA, Terjung RL. Phosphate uptake in rat skeletal muscle is reduced during isometric contractions. J Appl Physiol 2004;97(1):57–62. [PubMed: 14990549]
13. Germinario E, Esposito A, Midrio M, Peron S, Palade PT, Betto R, Danieli-Betto D. High-frequency fatigue of skeletal muscle: role of extracellular Ca(2+). Eur J Appl Physiol 2008;104(3):445–453. [PubMed: 18560877]
14. Lansman JB, Franco-Obregon A. Mechanosensitive ion channels in skeletal muscle: a link in the membrane pathology of muscular dystrophy. Clin Exp Pharmacol Physiol 2006;33(7):649–656. [PubMed: 16789935]
15. Nickerson JG, Momken I, Benton CR, Lally J, Holloway GP, Han XX, Glatz JF, Chabowski A, Luiken JJ, Bonen A. Protein-mediated fatty acid uptake: regulation by contraction, AMP-activated protein kinase, and endocrine signals. Appl Physiol Nutr Metab 2007;32(5):865–873. [PubMed: 18059611]
16. Wu PI, Edelman ER. Structural biomechanics modulate intramuscular distribution of locally delivered drugs. J Biomech 2008;41(13):2884–2891. [PubMed: 18706562]
17. Carpenter AE, Jones TR, Lamprecht MR, Clarke C, Kang IH, Friman O, Guertin DA, Chang JH, Lindquist RA, Moffat J, Golland P, Sabatini DM. CellProfiler: image analysis software for identifying and quantifying cell phenotypes. Genome Biol 2006;7(10):R100. [PubMed: 17076895]
18. Keener, J.; Sneyd, J. Mathematical physiology. Springer-Verlag; New York: 1998.
19. Chen KC, Nicholson C. Changes in brain cell shape create residual extracellular space volume and explain tortuosity behavior during osmotic challenge. Proc Natl Acad Sci U S A 2000;97(15):8306–8311. [PubMed: 10890922]
20. Bensoussan, A.; Lions, JL.; Papanicolaou, G. Asymptotic Analysis for Periodic Structures. North Holland Science Publishers; New York: 1978.
21. McCarthy MJ, Soong DS, Edelman ER. Control of Drug Release From Polymer Matrices Impregnated with Magnetic Beads - A Proposed Mechanism and Model for Enhanced Release. J Controlled Release 1984;1:143–147.
22. Thomas AM, Narayanan R. Physics of oscillatory flow and its effect on the mass transfer and separation of species. Phys Fluids 2001;13(4):859–866.
23. Azer K. Taylor diffusion in time-dependent flow. Int J Heat Mass Tran 2005;48(13):2735–2740.
24. Fung, YC. Biomechanics: mechanical properties of living tissues. Springer-Verlag; New York: 1993.
25. Formaggia L, Nobile F. A stability analysis for the arbitrary lagrangian eulerian formuation with finite elements. East-West J Numer Math 1999;7(2):105–131.
26. Hill DK. The organization of the inter-fibre space in the striated muscle of the toad, and the alignment of striations of neighbouring fibres. J Physiol (Lond) 1965;179(2):368–384. [PubMed: 5322820]
27. Kobayashi N, Yonemura K. The extracellular space in red and white muscles of the rat. Jap J Physiol 1967;17(6):698–707. [PubMed: 5300935]
28. Gajdosik RL. Passive extensibility of skeletal muscle: review of the literature with clinical implications. Clin Biomech 2001;16(2):87–101.
29. Rutili G, Arfors KE. Fluorescein-labelled dextran measurement in interstitial fluid in studies of macromolecular permeability. Microvasc Res 1976;12(2):221–230. [PubMed: 979669]
30. Rasgado-Flores H, Taylor SR, Pena-Rasgado C, Orgel J, Gonzalez-Serratos H. Muscle contraction and cell volume changes in skeletal muscle. J Muscle Res Cell Motil 2004;25(8):592–595. [PubMed: 16118848]
31. Davis J, Kaufman KR, Lieber RL. Correlation between active and passive isometric force and intramuscular pressure in the isolated rabbit tibialis anterior muscle. J Biomech 2003;36(4):505–512. [PubMed: 12600341]
32. Sejersted, OM.; Hargens, AR. Fatigue. Gandevia, SC., editor. Plenum Press; New York: 1995. p. 339-350.
33. Wisnes A, Kirkebo A. Regional distribution of blood flow in calf muscles of rat during passive stretch and sustained contraction. Acta Physiol Scand 1976;96(2):256–266. [PubMed: 1258671]
34. Ward DS, Hamilton MT, Watson PD. Measurement of tissue volume during non-steady state high-intensity muscle contraction. Am J Physiol 1996;271(6 Pt 2):R1682–1690. [PubMed: 8997370]

35. Nara E, Saikawa A, Masegi M, Hashida M, Sezaki H. Contribution of interstitial diffusion in drug absorption from perfused rabbit muscle: effect of hyaluronidase on absorption. Chem Pharm Bull (Tokyo) 1992;40(3):737–740. [PubMed: 1611686]

36. Purslow PP. Strain-induced reorientation of an intramuscular connective tissue network: implications for passive muscle elasticity. J Biomech 1989;22(1):21–31. [PubMed: 2914969]

37. Purslow PP, Trotter JA. The morphology and mechanical properties of endomysium in series-fibred muscles: variations with muscle length. J Muscle Res Cell Motil 1994;15(3):299–308. [PubMed: 7929795]

38. Williams PE, Goldspink G. Connective tissue changes in immobilised muscle. J Anat 1984;138(Pt 2):343–350. [PubMed: 6715254]

39. Gauthier MG, Slater GW. Exactly solvable Ogston model of gel electrophoresis. IX. Generalizing the lattic model to treat high field intensities. J Chem Phys 2002;117(14):6745–6756.

40. Huijing PA. Muscle as a collagen fiber reinforced composite: a review of force transmission in muscle and whole limb. J Biomech 1999;32(4):329–345. [PubMed: 10213024]

41. Passerieux E, Rossignol R, Letellier T, Delage JP. Physical continuity of the perimysium from myofibers to tendons: involvement in lateral force transmission in skeletal muscle. J Struct Biol 2007;159(1):19–28. [PubMed: 17433715]

42. Grounds MD, Sorokin L, White J. Strength at the extracellular matrix-muscle interface. Scand J Med Sci Sports 2005;15(6):381–391. [PubMed: 16293150]

43. Ihlemann J, Ploug T, Galbo H. Effect of force development on contraction induced glucose transport in fast twitch rat muscle. Acta Physiol Scand 2001;171(4):439–444. [PubMed: 11421859]

44. Baker CH, Davis DL. Isolated skeletal muscle blood flow and volume changes during contractile activity. Blood Vessels 1974;11(1–2):32–44. [PubMed: 4614880]

45. Cappelli V, Reggiani C, Poggesi C, Ricciardi L. Inulin uptake and washout in contracting and quiescent rat papillary muscle. Arch Int Physiol Biochim 1982;90(4):231–236. [PubMed: 6188425]

46. Fannon M, Forsten KE, Nugent MA. Potentiation and inhibition of bFGF binding by heparin: a model for regulation of cellular response. Biochemistry 2000;39(6):1434–1445. [PubMed: 10684625]

47. Kanematsu A, Marui A, Yamamoto S, Ozeki M, Hirano Y, Yamamoto M, Ogawa O, Komeda M, Tabata Y. Type I collagen can function as a reservoir of basic fibroblast growth factor. J Control Release 2004;99(2):281–292. [PubMed: 15380637]

48. Lu H, Xu X, Zhang M, Cao R, Brakenhielm E, Li C, Lin H, Yao G, Sun H, Qi L, Tang M, Dai H, Zhang Y, Su R, Bi Y, Zhang Y, Cao Y. Combinatorial protein therapy of angiogenic and arteriogenic factors remarkably improves collaterogenesis and cardiac function in pigs. Proc Natl Acad Sci U S A 2007;104(29):12140–12145. [PubMed: 17636133]

49. Masuoka K, Ishihara M, Asazuma T, Hattori H, Matsui T, Takase B, Kanatani Y, Fujita M, Saito Y, Yura H, Fujikawa K, Nemoto K. The interaction of chitosan with fibroblast growth factor-2 and its protection from inactivation. Biomaterials 2005;26(16):3277–3284. [PubMed: 15603823]

50. Epstein SE, Kornowski R, Fuchs S, Dvorak HF. Angiogenesis therapy: amidst the hype, the neglected potential for serious side effects. Circulation 2001;104(1):115–119. [PubMed: 11435348]

51. Ingber DE. Tensegrity-based mechanosensing from macro to micro. Prog Biophys Mol Biol 2008;97 (2–3):163–179. [PubMed: 18406455]

52. Balcells M, Fernandez Suarez M, Vazquez M, Edelman ER. Cells in fluidic environments are sensitive to flow frequency. J Cell Physiol 2005;204(1):329–335. [PubMed: 15700266]

53. Nugent LJ, Jain RK. Plasma pharmacokinetics and interstitial diffusion of macromolecules in a capillary bed. Am J Physiol 1984;246(1 Pt 2):H129–137. [PubMed: 6198927]

APPENDIX A: HOMOGENIZATION THEORY

Transport through a complex medium composed of smaller repeating elements can be represented on multiple scales. For muscle tissues, micro-scale corresponds to the cellular or myofiber level while macro-scale corresponds to the tissue or muscle bundle level. On the cellular level, free diffusion is influenced by boundary conditions defined by cell geometry.

On the tissue level, transport occurs across a continuous medium. Diffusion of drug through muscle was studied using a multi-scale approach [19] starting with:

$$\frac{\partial c}{\partial t}=\nabla \cdot (D(\underline{X})\nabla c) \tag{A1}$$

Where $X = (X_1, X_2, X_3)$ denotes the three-dimensional coordinate system on the cellular level. The diffusivity tensor $D(X)$, which D_{int} defines on the cellular level, is a continuous function of the position X. $D(X) = 0$ inside muscle fibers where no diffusion occurs.

Homogenization was used to derive macro-scale behaviors in the tissue based on micro-scale phenomena. This technique accounted for spatial variations in drug concentration on the cellular level to characterize drug concentration profiles on the tissue level. As fibers in the muscle were considered repeating elements, a representative volume describing a periodic distribution of fiber elements that compose the macro-scale tissue was used. In our model, muscle fibers were represented by white diamond elements arranged in a staggered periodically repeating array, and diffusion occurred in the pink interstitial space between them (Fig. 1B). This idealized configuration was used to derive continuous tissue level behaviors by averaging, or "homogenizing," cellular level variations. The homogenized version of Eq. (A1) [20] on the tissue level was:

$$\frac{\partial \langle c \rangle}{\partial t}=D_{eff}^{ij}\frac{\partial^2 \langle c \rangle}{\partial x_i \partial x_j} \tag{A2}$$

where $x = (x_1, x_2, x_3)$ denotes the three-dimensional coordinate system on the tissue level, D_{eff} is the macroscopic diffusion coefficient, $\langle c \rangle$ is average concentration, and i,j = (1,2,3). Effective diffusivity assumed the following form [20]:

$$D_{eff}^{ij}=\frac{1}{V_P}\int_P \left(D(\underline{X})\delta_{ij} - D(\underline{X})\frac{\partial \chi^j}{\partial X_i}\right) d\underline{X} \tag{A3}$$

where V_p is the volume of the periodic unit P, which is used to represent the periodic distribution of myofibers, and δ_{ij} is the Kronecker delta. Homogenization takes place for $X = x/\kappa$ in the theoretical limit as $\kappa \rightarrow 0$, where κ is a small parameter representing the periodicity of repeating elements.

The small periodic component of concentration, χ, in the periodic unit satisfied the equation [20]:

$$\nabla^2 \chi = 0 \tag{A4}$$

with boundary conditions Γ_1, corresponding to the borders of interstitial space on the periodic unit, and Γ_2, corresponding to the interface between myofibers and the interstitial space. Symmetric ($\nabla\chi \cdot n = 0$) and periodic ($\chi = 0$) conditions were applied to components of Γ_1 that were parallel and perpendicular, respectively, to e [19]. The non-homogeneous Neumann condition: n

$$\underline{n} \cdot \nabla \chi = \underline{n} \cdot \underline{e} \tag{A5}$$

was applied to Γ_2 (Fig. 1C), where n is the outward unit normal vector on the fiber surface and e is the direction of macro-scale transport. The diffusion coefficient in the direction of e became:

$$\frac{D_{eff}}{D_{int}} = \frac{1}{V_P}\int_P (1 - \underline{e}\cdot\nabla\chi)\, d\underline{X} \tag{A6}$$

where D_{int} is interstitial diffusivity. As the axial length of our muscle sample was significantly greater than its radial cross-sectional area, the equations above were formulated in a two dimensional configuration and solved on a reduced computational domain Ω (Fig. 1B, *inset*), which served as the periodic unit P and sufficiently characterized the symmetrical aspects of the problem.

The dependence of D_{eff} on ϕ and fiber arrangement as they change with static strain was investigated by modeling D_1. D_2 in Eq. (1) accounts for the effects of interstitial fluid viscosity and possible hydrodynamic interactions of the drug with muscle fibers due to the relative size of the drug. Because the 3.2 nm hydrodynamic radius of 20 kDa dextran used in our experiments was two orders of magnitude less than the 0.43 μm minimum interstitial spacing between myofibers measured histologically in the soleus, D_2 was independent of ϕ. Also, it was assumed that *in vitro* incubated muscle samples were infiltrated by saline media and that the interstitial fluid had the physical characteristics of water. Thus, $D_{int} = D_w$, the free diffusivity of the drug in water, which is 1.026×10^{-4} mm^2/s for 20 kDa dextran [53]. With these assumptions, $D_2 = 1$ and Eq. (A6) became:

$$D_1 = \frac{D_{eff}}{D_w} = \frac{1}{A}\int_\Omega (1 - \underline{e}\cdot\nabla\chi)\, d\Omega \tag{A7}$$

APPENDIX B: AMPLITUDE OF RADIAL OSCILLATION

An elastic material satisfies the law:

$$\frac{\Delta V}{V} = \frac{\Delta L}{L}(1 - 2\nu) \tag{B1}$$

where ΔV is the change in total volume, ν is the Poisson ratio, and ΔL is the change in axial length. The Poisson ratio is defined as the ratio between the transverse, ε_{tr}, and axial strain, ε_{ax}:

$$\nu = -\frac{\varepsilon_{tr}}{\varepsilon_{ax}} = -\frac{\frac{\Delta R}{R}}{\frac{\Delta L}{L}} \tag{B2}$$

For an incompressible material, whose Poisson ratio is 0.5, volume is conserved during deformation, and no volume change occurs with axial strain according to Eq. (B1).

Thus, for a cylindrical sample of nominal radius R0 and length L0:

$$\Delta V = \pi R^2 L - \pi R0^2 L0 = 0 \tag{B3}$$

where R and L are the radius and the length, respectively, of the sample after deformation. R was determined by:

$$R=R0\sqrt{\frac{L0}{L}} \tag{B4}$$

The length and radius at each mean strain, n, were:

$$\begin{aligned} Ln&=L0+n\%L0\\ Rn&=R0\sqrt{\frac{1}{1+n\%}} \end{aligned} \tag{B5}$$

where L0 and R0 are the nominal length and radius, respectively, of the muscle, and n = 0, 5, 10, and 20, corresponding to the value of axial strain.

For cyclic strains, the maximum and minimum values for length and radial deformations were:

$$\begin{aligned} L_D&=Ln\pm 0.025*L0\\ R_D&=Rn\sqrt{\frac{Ln}{Ln\pm 0.025*L0}} \end{aligned} \tag{B6}$$

where n = 0, 5, 10, and 20. The absolute value of the amplitude of radial deformation during cyclic strain was:

$$\Delta R=|Rn-R_D| \tag{B7}$$

APPENDIX C: ARBITRARY LAGRANGIAN EULERIAN FORMULATION

During cyclic strain, the boundary of the radial section moved according to the exact sinusoidal function:

$$r(t)=Rn\sqrt{\frac{Ln}{Ln+0.025*L0*\sin(\omega t)}} \tag{C1}$$

derived from Eq. (B6). To simply terms, this relationship can be expressed in reference to the mean radius Rn, such that:

$$r(t)=Rn(1+\alpha\sin(\omega t)) \tag{C2}$$

where α is the radial strain amplitude relative to Rn:

$$\alpha=\frac{\Delta R}{Rn}, \tag{C3}$$

r(t) is the radial coordinate in the moving domain, $\Omega_D(r,\theta,t) = \{0 \le r(t) \le Rn\ (1 + \alpha \sin(\omega t)), 0 < \theta \le 2\pi\}$. And, R is the radial coordinate in the reference domain, $\Omega_0(R,\Theta) = \{0 \le R \le Rn, 0 < \Theta \le 2\pi\}$.

The transport equation was:

$$\frac{\partial c}{\partial t} - D_{eff}\nabla^2 c = 0 \quad \text{in } \Omega_D(t) \tag{C4}$$

which was formulated on Eulerian coordinates such that:

$$\frac{\partial c}{\partial t}\Big|_{\Omega_0} - D_{eff}\nabla^2 c - \underline{w}\cdot\nabla c = 0 \quad \text{in } \Omega_D(t) \tag{C5}$$

where w is the oscillatory velocity of the domain $\Omega_D(t)$.

Using cylindrical coordinates (r,θ) and considering the symmetry of the problem in θ, Eq. (C5) was written as:

$$\frac{\partial c}{\partial t}\Big|_{\Omega_0} - D_{eff}\nabla^2 c - w_r\frac{\partial c}{\partial r} = 0 \quad \text{in } \Omega_D(t) \tag{C6}$$

where w_r is the radial component of w, and reformulated in the reference domain Ω_0 with the boundary conditions as follows:

$$\begin{cases} \frac{\partial c}{\partial t} - \frac{D_{eff}}{(1+\alpha\sin(\omega t))^2}\nabla^2 c - \frac{R\omega\alpha\cos(\omega t)}{1+\alpha\sin(\omega t)}\frac{\partial c}{\partial R} = 0 & in\ \Omega_0 \\ c(t) = c_0 & R = R_0, t > 0 \\ c = 0 & 0 \le R < R_0, t = 0 \end{cases} \tag{C7}$$

Concentration at the final time was computed by averaging over the final period as follows:

$$c(R,T_f) = \frac{\int_{T1}^{T2} c(R,t)\,dt}{T2 - T1} \tag{C8}$$

where $T_1 = T_f - (T/2)$, $T_2 = T_f + (T/2)$, T is the period of a cycle, and R is the radial coordinate used to describe the domain Ω_0.

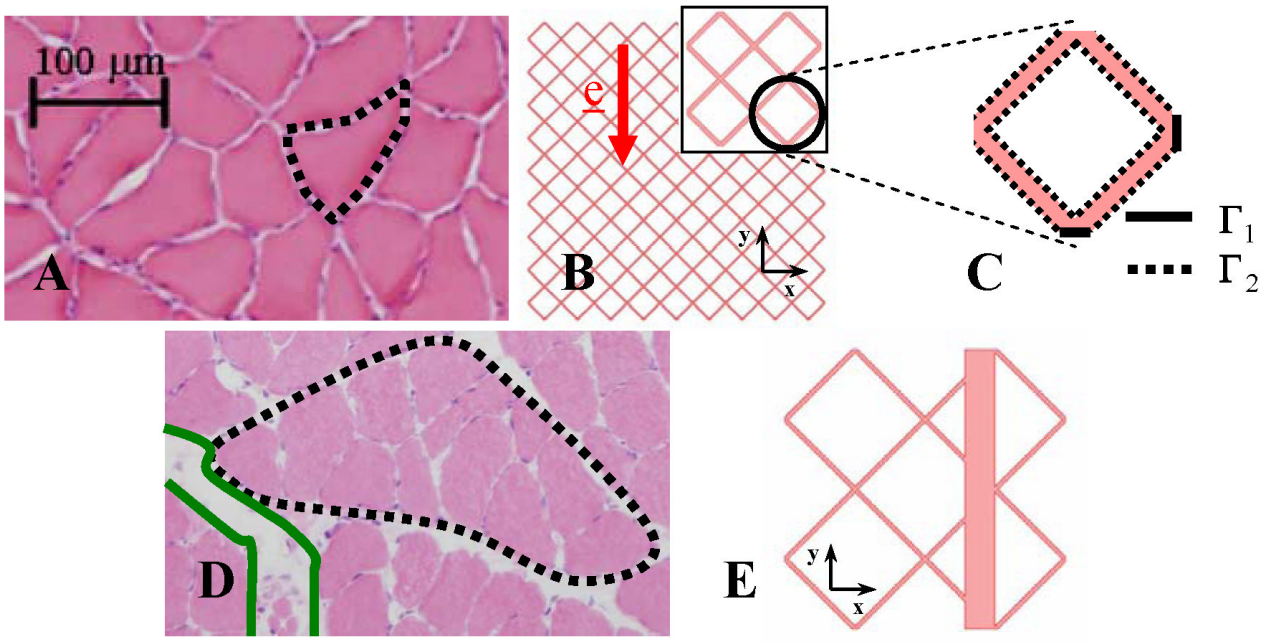

Fig. 1.

Static model. (A) HE image of a soleus axial cross-section showing the isotropic and homogeneous porous architecture and uniform interstitial spacing under 0% and 20% strains. A myofiber is outlined. (B) Two dimensional depiction of the homogeneous muscle axial cross-section with myofibers idealized by a regularly repeating lattice of staggered diamonds (*white*) interspaced with interstitial channels (*pink*) of consistent width. Symmetry of the problem allowed the computation to be carried out on a reduced domain, Ω, formed by a single lattice arrangement of diamonds (*inset*) with (C) boundaries Γ_1 and Γ_2. (D) HE image of the inhomogeneous fiber arrangement with wide interstitial channels (*green*) separating fascicles (*black*) of myofibers that occur under 5%, 10%, and 15% strains. (E) Depiction of the inhomogeneous muscle cross-section with a wide interstitial channel added to the regular lattice. Location of the channel with respect to the diamonds did not significantly influence transport.

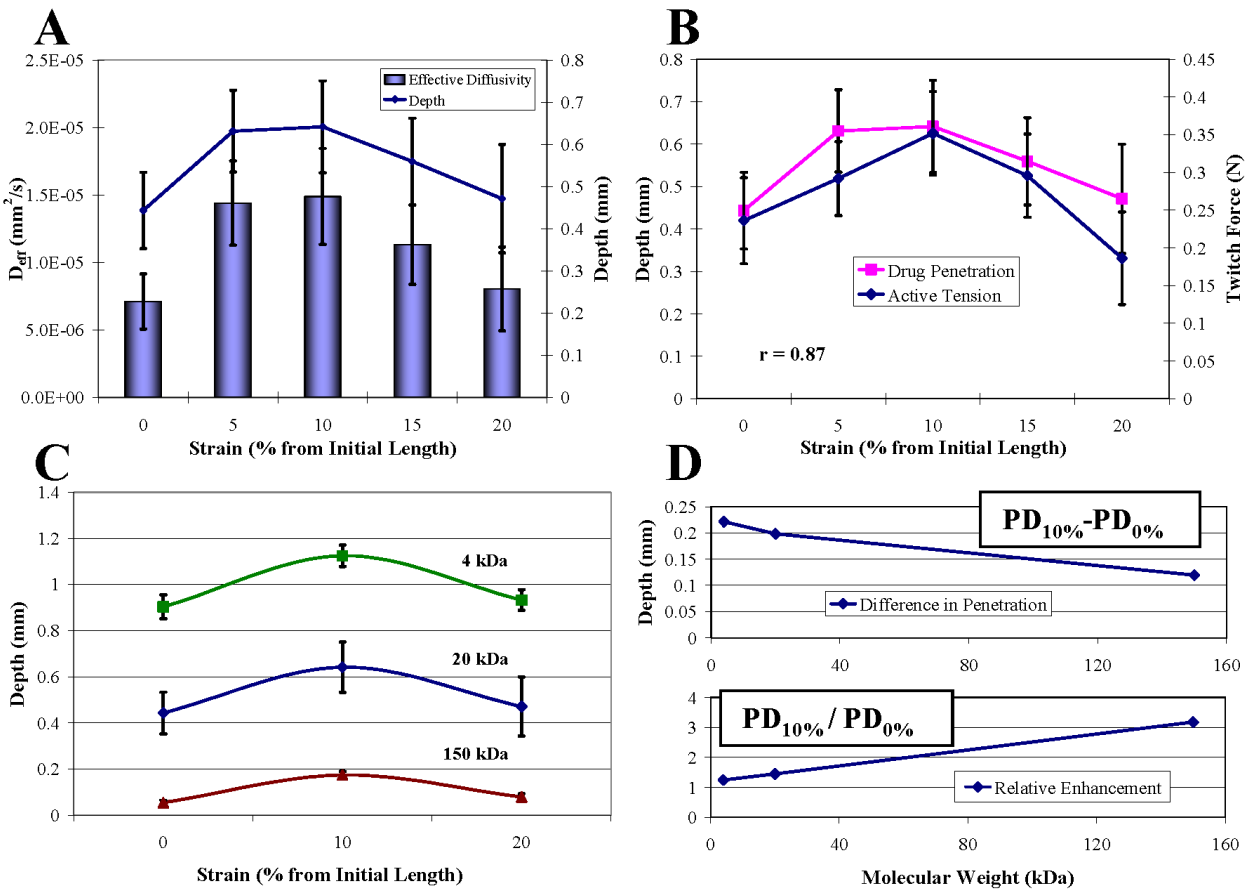

Fig. 2.

Drug transport under static strain. (A) Penetration depth and effective diffusivity of 20 kDa FITC-dextran in soleus over 0–20% strains increased significantly from baseline at 0% to a maximum at 10% (T-test, $p<0.05$). (B) Penetration correlated with isometric twitch force ($r = 0.87$). (C) Penetration decreased with increasing MW (Two-Factor ANOVA, $p<0.05$ between strains, $p<0.05$ between MWs). 4 kDa dextrans penetrated 2- and 10-fold farther than 20 kDa and 150 kDa dextrans, respectively, at each strain. (D) While the difference between penetration at 10% and 0% strain decreased, the ratio of penetration increased with MW.

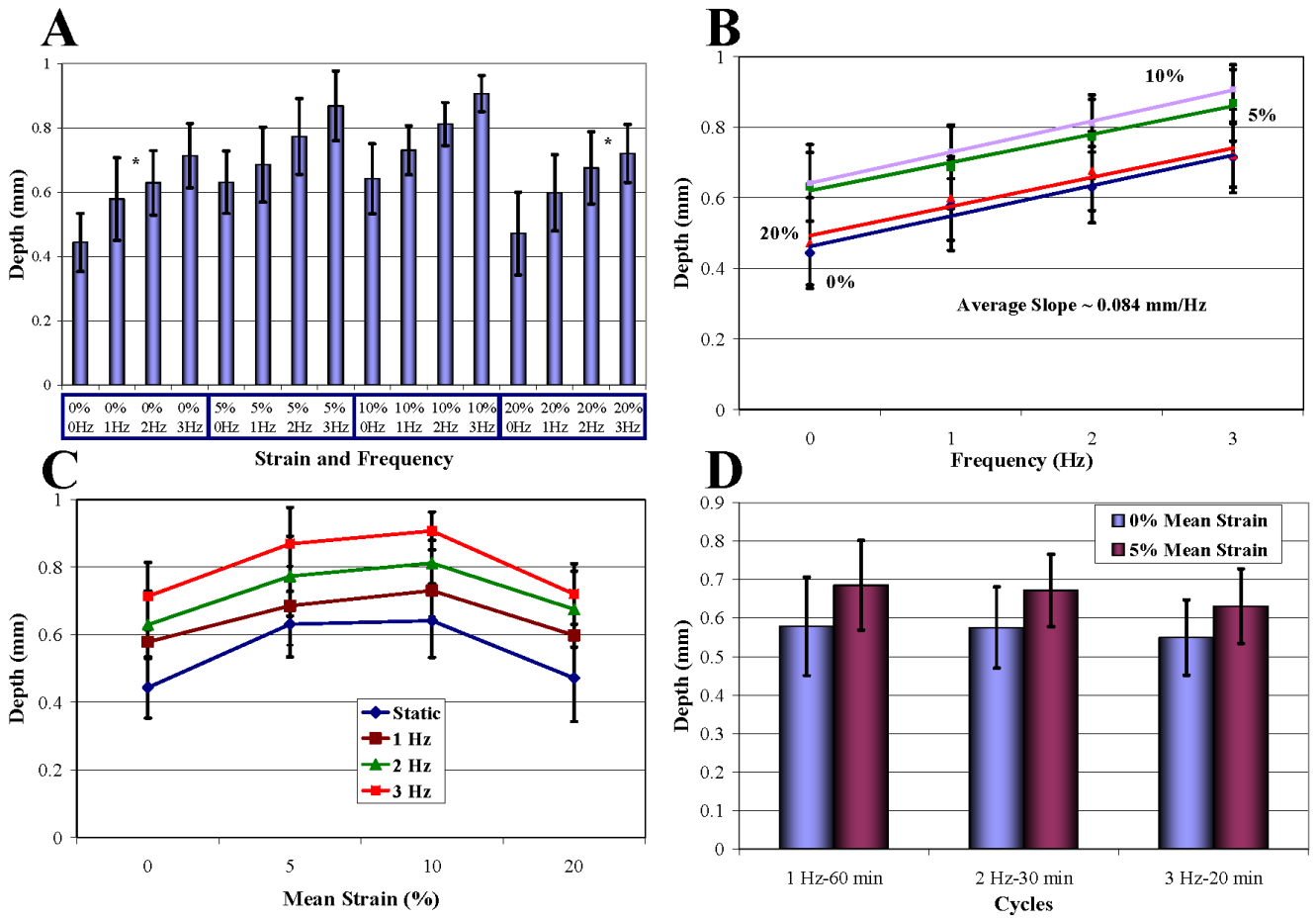

Fig. 3.

Impact of cyclic strain on drug penetration. (A) Cyclic loading significantly increased penetration linearly proportionally to loading frequency (T-test, $p<0.05$ except groups with * in between). 0 Hz groups are static cases in Fig. 2 A. (B) Slopes of the linear relationship between penetration and loading frequency at each mean strain were statistically the same (Single-Factor ANOVA, $p>0.05$). (C) Penetration profiles at each loading frequency. (D) Penetration at each strain was directly dependent on the number of loading cycles (Two-Factor ANOVA, $p<0.05$ between 0% and 5%, $p>0.05$ among loading groups). 1 Hz-60 min groups are those in Fig. 3A.

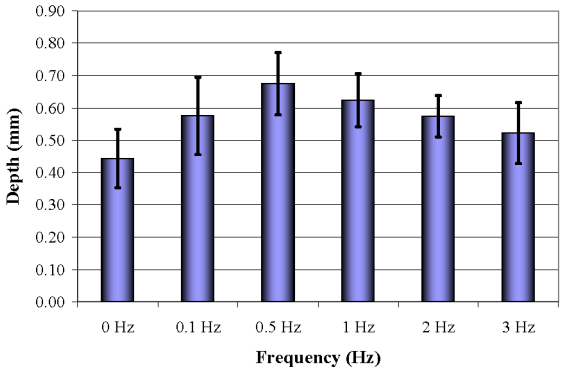

Fig. 4.
Impact of contraction on drug penetration. 0 Hz is 0% in Fig. 2A.

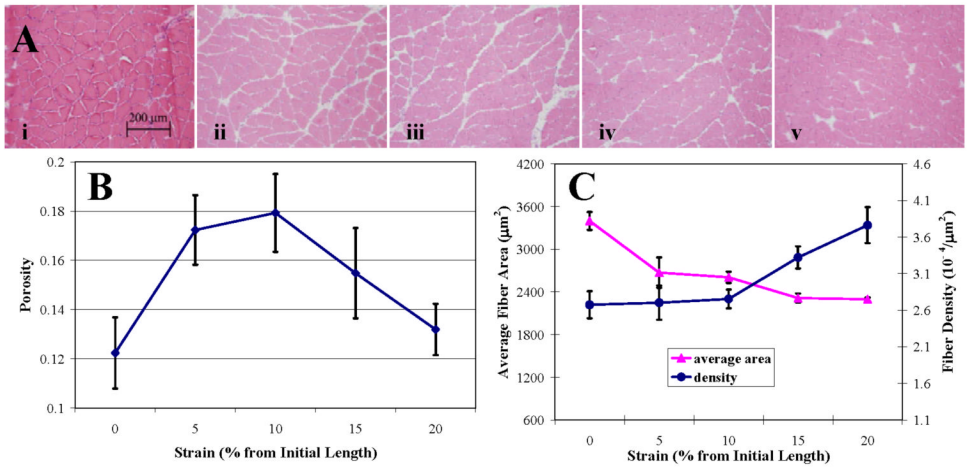

Fig. 5.

Architectural parameters over 0–20% strain. (A) HE stained axial cross-sections of soleus under (i) 0%, (ii) 5%, (iii) 10%, (iv) 15%, and (v) 20% static strain. (B) Porosity profile over strain. (C) Myofiber cross-sectional area and density changed inversely with strain.

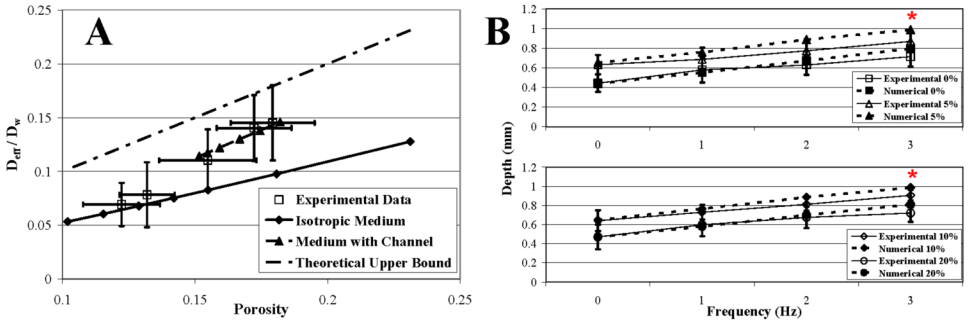

Fig. 6.

Numerical results. (A) Numerical and experimental results of effective diffusivity (D_{eff}/D_w) versus porosity (ϕ) over 0–20% strains. The upper limit of diffusivity, $D_{eff}/D_w = \phi$, represents transport along the myofiber axis through straight channels that occupy a fraction ϕ of the total area. Calculated channel sizes used in the numerical plot of *Medium with Channel* were 23–30% of myofiber sizes, predicting widths of 11–15 μm, which approximate empirical measurements. (B) Dynamic loading enhanced drug penetration through dispersion. Plots of 0%, 5%, 10%, and 20% mean strains. (*) Numerical results lie within the confidence limits of experimental data. Consideration of an elliptical muscle cross-sectional geometry, compressibility of the interstitial space, bulk interstitial fluid movement, and muscle viscoelasticity in a more complex model may more completely characterize transport effects produced by dynamic loading.

TABLE OF SYMBOLS IN COMPUTATIONAL MODEL

Symbol	Definition	Units
α	normalized amplitude of radial deformation during cyclic stretch, $\Delta R/Rn$	
$c(r,t)$	concentration of the drug in the tissue	(g/mm^3)
$\langle c \rangle$	average concentration in the periodic unit	(g/mm^3)
$\chi(x,y)$	the small periodic component of the macroscopic drug concentration field	
δ_{ij}	Kronecker delta	
$D(X)$	diffusivity tensor of the drug in the extracellular space	(mm^2/s)
D_{eff}	effective diffusion coefficient of the drug in the tissue (in the direction e)	(mm^2/s)
D_{int}	diffusion coefficient of the drug in the interstitial space	(mm^2/s)
D_w	free diffusion coefficient of the drug in water	(mm^2/s)
D_1	dimensionless reducing factor of D_w due to porosity and fiber arrangement	
D_2	dimensionless reducing factor of D_w due to interstitial characteristics	
e	direction of macroscopic diffusion	
ε_{ax}	axial strain	
ε_{tr}	transverse strain	
Γ_1	symmetric and periodic boundaries of Ω	
Γ_2	boundaries of Ω at the fiber interface with the interstitial space	
κ	periodicity of myofibers on the microscopic level	
ΔL	change in length of the muscle	(mm)
Ln	length of the muscle at the mean strains defined by index n	(mm)
ν	Poisson ratio	
n	index of mean strains = 0, 5, 10, 20	
n	outward unit normal vector at the solid boundaries, fiber surfaces, of Ω	
ω	radial frequency of pulsation of Ω_D	(rad/s)
$\Omega(x,y)$	computational domain for solving the homogenized equation of the static model	
$\Omega_D(r, \theta,t)$	computational domain for the dynamic model	
$\Omega_0(R,\Theta)$	reference domain used in the ALE formulation of the transport equation	
ϕ	tissue porosity; the ratio of the area or volume of interstitial space to the total area or volume, respectively, of the tissue	
P	periodic unit	
r(t)	radius of the muscle cross-section in Ω_D	(mm)
R	radius of the muscle cross section in Ω_0	(mm)
ΔR	amplitude of radial deformation during cyclic stretch	(mm)
R_D	maximum or minimum radius of the muscle section during cyclic stretching	(mm)
Rn	radius of the muscle at the mean strains defined by index n	(mm)
t	time	(s)
T	period of pulsation of Ω_D	(s)
T_f	simulation time (3600s)	(s)
V	initial volume of the muscle	(mm^3)

Symbol	Definition	Units
ΔV	change in volume of the muscle	(mm^3)
V_P	volume of the periodic unit	(mm^3)
w	velocity vector of the moving domain Ω_D	(mm/s)
w_r	radial component of the velocity vector w	(mm/s)
$X=(X_1, X_2, X_3)$	Cartesian coordinate system used to describe the microscopic scale	
$x= (x_1, x_2, x_3)$	Cartesian coordinate system used to describe the periodic unit $\Omega(x,y)$	